Energy Proceedings
Vol 43, 2024
ISSN 2004-2965

The temperature measurement of hydrogen flame based on CCD and IR images

Jianan Yin[1], Changqing Dong[1,2,*],Junjiao Zhang[3],Xiaoying Hu[1],Junjie Xue[1],Ying Zhao[1],Xiaoqiang Wang[1]

1 National Engineering Laboratory for Biomass Power Generation Equipment, School of New Energy, North China Electric Power University, Beijing 102206, China

2 State Key Laboratory of Alternate Electrical Power System with Renewable Energy Sources, North China Electric Power University, Beijing 102206, China
(*School of Energy, Power and Mechanical Engineering, North China Electric Power University, Beijing 102206, China
*Corresponding author: dongcq@ncepu.edu.cn)

ABSTRACT

This study explored the relationship between the RGB color space and the temperature of hydrogen flames with thermal reflection principles. The prediction model based on CCD and infrared (IR) image were compared. The model based on RGB difference as inputs for CCD image showed an average relative error of 9.8314%. The model based on infrared image RGB values showed an average relative error of 6.6652%.

Keywords: hydrogen flame, temperature measurement, CCD, infrared image

1. INTRODUCTION

Hydrogen is an important clean energy source for carbon neutrality and it is colorless, odorless, inflammable, and explosive in certain concentrations [1].

In order to monitor the flame combustion, acoustic method [2-4], thermodynamic method [5] and optical method [6-13] can be used. While the radiation of hydrogen flame was mainly in the range of UV band. The traditional visible and far infrared band (>1500 nm) method based on spectral radiation distribution face a lot of challenge [14-15].

This study was aimed to establish a new temperature prediction model based on thermal reflection principles [16-20], linking the RGB color space of visible light images and infrared images to the temperature of hydrogen flame.

2. MATERIAL AND METHODS

The hydrogen was generated with an HGH-500 hydrogen generator and combusted in the air (the ambient temperature was 32.2°C) through a 1.5-millimeter-diameter copper tube burner. A stainless-steel plate, positioned 10 millimeters behind the copper tube burner, served as the wall. The combustion process was monitored with a CCD camera and an infrared thermal imaging camera as shown in Fig 1.

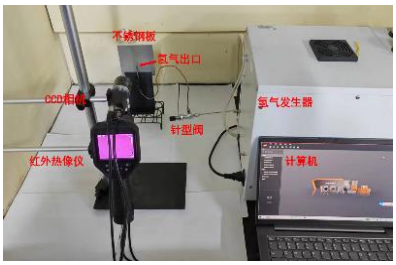

Fig. 1. experimental placement

Two K-type thermocouples, labeled as points A (60mm above the burner) and B (30mm below the burner), were used to measure the temperature changes. The hydrogen gas flow rate was adjusted sequentially from 0 mL/min to 500 mL/min. After each adjustment, a 5-minute waiting period ensured temperature stability. Temperature of the thermocouples were recorded every 30 seconds. CCD visible light images (631×536 pixels) and infrared images (361×311 pixels) were taken at the same time.

3. RESULTS AND DISCUSSION

3.1 Color moment and temperature correlation analysis

The Pearson correlation coefficient between the first and second moments of RGB and temperature were calculated and showed in Table 1. It showed that there was strong relationship between RGB color space components and temperature.

Table 1 Correlation coefficients between moments and temperature in RGB color space

This is a paper for 15th International Conference on Applied Energy (ICAE2023), Dec. 3-7, 2023, Doha, Qatar.

Each color characteristic		*Correlation coefficient*
R	array of first-order moments	0.9688
	array of second-order moments	0.9276
G	array of first-order moments	0.7454
	array of second-order moments	0.6994
B	array of first-order moments	0.9503
	array of second-order moments	0.9320

3.2 Model Based on RGB Color Space

3.2.1 Flame area recognition

In the non-flame regions, the images only captured the reflection and radiation from the stainless-steel plate wall. In the flame regions, the images received reflection and radiation from both the stainless-steel plate and the hydrogen flame. There was a great change of RGB values at the edges of the flames. And an inflection point detection method was used to delineate the boundaries of the flame region. The variation of R value for the 164th and 221st rows was depicted in Fig.2 (a). The second derivative curve portraying of the R value variation for the 164th row was showed in Fig. 2(b). According the R value variation, the flame regions were separated for both visible light and infrared and images.

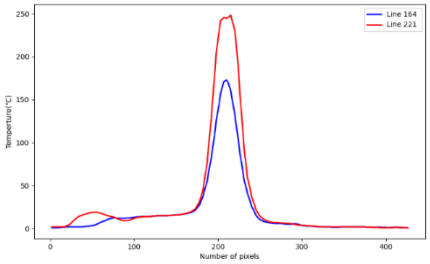

(a) Smoothed curve

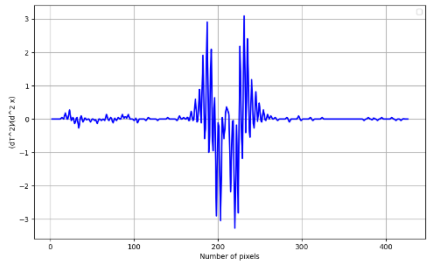

(b) Second derivative curve

Fig. 2 Smoothed curve and second derivative curve

3.2.2 The temperature prediction model based on the RGB values of the CCD visible light image.

The functional relationship between temperature (measured by thermocouples at points A and B) and the corresponding RGB values and RGB differences in the visible light images were analyzed and a three-variable linear regression model with thermocouple temperature as the true flame temperature baseline was showed in equation 1 and 2 based A point data. The fitting errors for points A and B are shown in table 2.

Table 2 The comparison between the fitting errors for points A and B and the fitting performance

	MAE	MRE	RMSE	R^2
A	31.89	0.132	39.91	0.94
B	57.36	0.108	77.73	0.79
A1	31.90	0.132	39.91	0.94
B1	57.36	0.108	77.73	0.79

*Where mean absolute error was abbreviated as MAE, root mean square error as RMSE, mean relative error as (MRE), and coefficient of determination as R2. A and B refers to using RGB as input. A1 and B1 refer to using RGB difference as input.

The temperature of the flame area was calculated with Equation 1 (with RGB values as inputs) and Equation 2 (with RGB differences as inputs):

$$\begin{cases} T_{xz(i,j)} = 15.312R_{0(i,j)} + 34.179G_{0(i,j)} + 22.629B_{0(i,j)} - 6140.2 & L_{(i,0)} \le i \le L_{(i,1)} \\ T_{xz(i,j)} = 32 & i < L_{(i,0)}, i > L_{(i,1)} \end{cases} \quad (1)$$

$$\begin{cases} T_{xz(i,j)} = 15.312\Delta R_{0(i,j)} + 34.179\Delta G_{0(i,j)} + 22.629\Delta B_{0(i,j)} + 72.442 & L_{(i,0)} \le i \le L_{(i,1)} \\ T_{xz(i,j)} = 32 & i < L_{(i,0)}, i > L_{(i,1)} \end{cases} \quad (2)$$

Where :

$T_{xz(i,j)}$—The predicted temperature at (i,j) ,(℃);

$R_{0(i,j)}, G_{0(i,j)}, B_{0(i,j)}$—The R,G,B value at (i,j);

$\Delta R_{0(i,j)}, \Delta G_{0(i,j)}, \Delta B_{0(i,j)}$ —The difference of R,G,B ;

$L_{(i,0)}$—The left boundary in the i-th row;

$L_{(i,1)}$ —The right boundary in the i-th row。

Fig.3 showed the temperature distribution maps corresponding to the predicted temperature matrices.

For the model based on visible light images with RGB values as inputs, anomalies were observed with higher temperatures above the flame and lower temperatures in the core of the flame. This phenomenon can be attributed to two main factors: (1) the influence of the background plate wall and (2) the effect of environmental lighting. Therefore, when predicting hydrogen flame temperatures using CCD images, the method of utilizing RGB differences in the images appears to be more reasonable and yields improved prediction results.

Under conditions of a hydrogen gas flow rate of 500 ml/min, the measured temperatures at various positions within the hydrogen flame and predicted value based on CCD image RGB differences were copmared and showed in Fig. 4. For each pixel position, the thermocouple temperature was considered as the ground truth temperature. The average relative error across the 16 pixel positions in the predicted temperature matrix is 9.8314%, and the root mean square error is 49.3470.

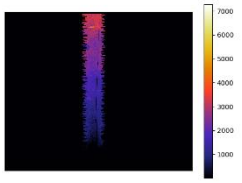

(a) RGB values as input

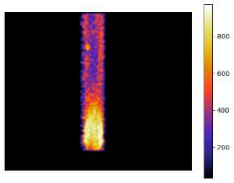

(b) RGB difference as input

Fig.3 Temperature prediction distribution for the hydrogen flow rate of 500 ml/min

Fig. 4 (a) The positions of the thermocouple temperature measurement pixels

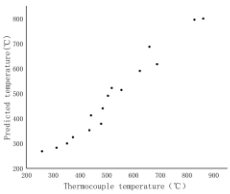

Fig.4 (b) Scatter plot of thermocouple temperature and predicted temperature

3.2.3 Temperature prediction model based on RGB of infrared thermal imager images

Using the same method as described in Section 3.2.2, temperature analysis and prediction were performed with the infrared images. The fitting errors for points A and B are shown in table 3.

Table 3 The comparison between the fitting errors for points A and B and the fitting performance

	MAE	MRE	RMSE	R^2
A	17.51	0.036	43.84	0.91
B	23.60	0.067	27.17	0.97
A1	17.51	0.036	43.84	0.91
B1	23.61	0.067	27.17	0.97

The temperature of the flame area was calculated with Equation 3 (with RGB values as inputs) and Equation 4 (with RGB differences as inputs):

$$\begin{cases} T_{xz(i,j)} = 2.094R_{0(i,j)} + 1.355G_{0(i,j)} + 0.7624B_{0(i,j)} \\ \quad -102.93 \qquad L_{(i,0)} \le i \le L_{(i,1)} \\ T_{xz(i,j)} = 32 \qquad i < L_{(i,0)}, i > L_{(i,1)} \end{cases} \tag{3}$$

$$\begin{cases} T_{xz(i,j)} = 2.094\Delta R_{0(i,j)} + 1.355\Delta G_{0(i,j)} + 0.7624\Delta B_{0(i,j)} \\ \quad +718.36 \qquad L_{(i,0)} \le i \le L_{(i,1)} \\ T_{xz(i,j)} = 32 \qquad i < L_{(i,0)}, i > L_{(i,1)} \end{cases} \tag{4}$$

The predicted temperature distribution diagram is shown in Fig.5. The temperature prediction based on infrared images was more accurate when RGB values were used as input. When using the RGB differences between infrared images and ambient temperature images as input for temperature prediction at different hydrogen flow rates, the resulting temperature distribution map exhibits a band-like pattern of lower temperatures within the flame region. The reason for this phenomenon was that at ambient temperature, the strip-like low-temperature region corresponds to the reflective area of the thermal imager. The reflective area of the thermal imager does not conform to the assumptions of the model, which reduces the credibility of using RGB differences as input for the prediction model.The pixel positions for temperature measurement were shown in Figure 6, with a total of 16 positions. The average relative error between the predicted temperature and the actual temperature using the RGB value of the infrared image as input was 6.6652%,and the root mean square error was 37.1759.

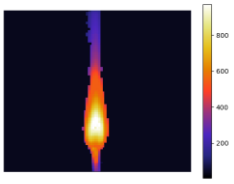

(a) RGB values as input

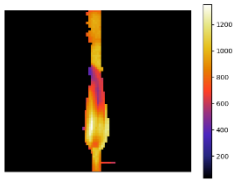

(b) RGB difference as input

Fig. 5 Temperature prediction distribution for the hydrogen flow rate of 500 ml/m*i*

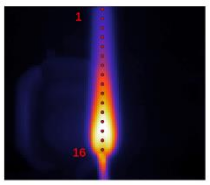

Fig. 6 (a) The positions of the thermocouple

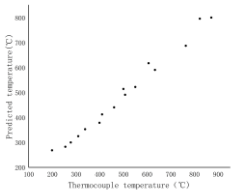

Fig. 6 (b) Scatter plot of thermocouple

temperature measurement pixels	temperature and predicted temperature

4. CONCLUSIONS

To address temperature measurement complexities in low-emissivity hydrogen flames, the thermal reflection principles were used in this study. Two methods: (1) using RGB components as input to study their relationship with temperature, and (2) using the differences between RGB components and room temperature images as input to study their relationship with temperature were carried out.

It was showed that CCD images was significantly affected by the environment, and with RGB difference (method 2) as input achieved higher prediction accuracy (average relative error of 9.8314%). The reflective region of the thermal imager has a significant impact on infrared images, therefore, Method 1 exhibited higher prediction accuracy(average relative error of 6.6652%).

REFERENCE

[1] SHAO Zhigang, YI Baolian. Developing Trend and Present Status of Hydrogen Energy and Fuel Cell Development. Bulletin of Chinese Academy of Sciences 2019, 34(4): 469-477.

[2] Truffin K, Poinsot T. Comparison and extension of methods for acoustic identification of burners. Combustion and Flame 2005;142(4):388–400.

[3] Le Helley P. Etude théorique et expérimentale des instabilités de combustion et de leur contrôle dans un brûleur laminaire prémélangé. Châtenay-Malabry, Ecole centrale de Paris; 1994.

[4]Kaufmann A, Nicoud F, Poinsot T. Flow forcing techniques for numerical simulation of combustion instabilities. Combustion and Flame 2002;131(4): 371–-385.

[5] Sujatha K, Venmathi M, Pappa N. Flame Monitoring in power station boilers using image processing. ICTACT Journal on Image and Video Processing 2012;2(4):427–434.

[6] Arias L, Torres S, Sbarbaro D, et al. Photodiode-based sensor for flame sensing and combustion-process monitoring. Applied optics 2008;47(29): 5541–5549.

[7] Romero C, Li X, Keyvan S, et al. Spectrometer-based combustion monitoring for flame stoichiometry and temperature control. Applied Thermal Engineering 2005;25(5-6):659–676.

[8] Wójcik W. Application of fibre-optic flame monitoring systems to diagnostics of combustion process in power boilers. Bulletin of the Polish Academy of Sciences: Technical Sciences 2008:177–195.

[9] Wang F, Wang X J, Ma Z Y, et al. The research on the estimation for the NOx emissive concentration of the pulverized coal boiler by the flame image processing technique. Fuel 2002;81(16):2113–2120.

[10] Chi T, Zhang H, Yan Y, et al. Investigations into the ignition behaviors of pulverized coals and coal blends in a drop tube furnace using flame monitoring techniques. Fuel 2010;89(3):743–751.

[11] Zou C, Cai L, Wu D, et al. Ignition behaviors of pulverized coal particles in O_2/N_2 and O_2/H_2O mixtures in a drop tube furnace using flame monitoring techniques. Proceedings of the Combustion Institute 2015; 35(3):3629–3636.

[12] Sarroza A C, Bennet T D, Eastwick C, et al. Characterising pulverised fuel ignition in a visual drop tube furnace by use of a high-speed imaging technique. Fuel Processing Technology 2017; 157: 1–11.

[13] Wang M, Ye Q, Yuan Z. A temperature measurement method based on visible light chromaticity index and k-nearest neighbors algorithm. 2019 PhotonIcs & Electromagnetics Research Symposium-Spring (PIERS-Spring). IEEE 2019: 1467–1472.

[14] Arens E E , Youngquist R C , Starr S O . Intensity calibrated hydrogen flame spectrum. International Journal of Hydrogen Energy 2014; 39(17):9545-9551.

[15]Zheng S, Cai W, Zhao C, et al. On the measurement of flame temperature and emissivity based on multispectral imaging technique. Measurement 2022; 196: 111272.

[16] Liu Y, Zhai Y, Jing X, Ding L, Ren Y, Wu A. High Time-Resolution Transient Thermoreflectance Microscopic Thermal Imaging Apparatus. Spacecraft Engineering and Testing Technology 2022;42(5):73–78.

[17] Lu G, Yan Y, Colechin M. A digital imaging based multifunctional flame monitoring system. IEEE Transactions on instrumentation and measurement 2004;53(4): 1152–1158.

[18] Lu G, Yan Y, Cornwell S, et al. Impact of co-firing coal and biomass on flame characteristics and stability. Fuel 2008; 87(7): 1133–1140.

[19] Sawicki D. Determining of combustion process state based on flame images analysis using k-NN classification. Photonics Applications in Astronomy, Communications, Industry, and High Energy Physics Experiments 2017. SPIE 2017;10445: 1738–1744.

[20] Sun D, Lu G, Zhou H, et al. Flame stability monitoring and characterization through digital imaging and spectral analysis. Measurement Science and Technology 2011; 22(11):114007.